Boundary magnetization properties of epitaxial $Cr_{2-x}Al_xO_3$ thin films

Lorenzo Fallarino,[1,*] Christian Binek,[2] and Andreas Berger[1]

[1]*CIC nanoGUNE, Tolosa Hiribidea 76, 20018 Donostia-San Sebastian, Spain*

[2]*Department of Physics & Astronomy and Nebraska Center for Materials and Nanoscience,*
University of Nebraska, Lincoln, Nebraska 68588-0111, USA

The magnetoelectric antiferromagnet α-Cr_2O_3 (chromia) is known to possess a roughness insensitive net equilibrium magnetization at the (0001) surface, called boundary magnetization (BM), which is coupled to the bulk antiferromagnetic order parameter. In order to verify whether this symmetry sensitive BM persists in alloys, we investigate the impact of diamagnetic dilution on chromia thin films alloyed with the isostructural α-Al_2O_3 (alumina). Single-crystalline $Cr_{2-x}Al_xO_3$ thin films with (0001) surface orientation and varying stoichiometry have been grown by sputter codeposition in the concentration range between $x = 0$ and $x = 0.6$. For these samples, we find the corundum crystal structure, the antiferromagnetic ordering, and the boundary magnetization to be preserved. We also find that the critical temperature T_N can be tuned by alloying with α-Al_2O_3, using the BM as a probe to study the magnetic phase transition. Furthermore, we were able to evaluate the critical exponent and the absolute BM values for different samples. Both properties corroborate that the observed magnetic signals originate from the BM rather than the bulk of the samples.

PACS number(s): 75.50.Ee, 75.70.Ak, 75.70.Rf, 77.55.Nv

I. INTRODUCTION

The prediction by Dzyaloshinskii that in a class of antiferromagnetic insulators such as α-Cr_2O_3 (chromia), an electric (magnetic) polarization could be induced by applying an external magnetic (electric) field, and its subsequent observations, have recently attracted a lot of renewed attention [1–4]. The so-called magnetoelectric effect, for which the antiferromagnetic chromia represents the archetypical material, is due to the possibility to control the material's order parameter in response to an unconventional field combination. It is given by the joint action of a magnetic and an electric field in contrast to the conventional case of a standard ferromagnet where the magnetization is coupled to the magnetic field, and a simple ferroelectric where the polarization is manipulated by an electric field [5–8]. α-Cr_2O_3 has the highest Néel temperature ($T_N = 307$ K) among the well-characterized magnetoelectric antiferromagnets [4], which enables magnetoelectricity at room temperature but does not provide enough flexibility for practical applications. Magnetoelectric device applications strive to utilize voltage-controlled interface or boundary magnetization. This particular equilibrium interface property is symmetry allowed in systems where time-reversal and spatial-inversion symmetry are broken and their combined operation leaves the spin structure invariant. This is the case in a single-crystalline magnetoelectric antiferromagnet, which therefore can exhibit an equilibrium net magnetization at the boundary. In chromia, this boundary magnetization (BM) exists at the (0001) surface [9–11]. The BM is fully coupled to the bulk antiferromagnetic (AF) order parameter and can be reversed together with it by a combination of E and H fields in bulk materials [8]. In addition, the switching can take place in the presence of only a magnetic field for single-crystal (0001) oriented thin chromia films [12,13]. Hereby, the coercive field, $\mu_0 H_c$, shows a giant temperature

sensitivity, of the order of $|\mu_0 \frac{dH_C}{dT}| \approx 1$ T/K, which makes chromia-based materials highly attractive for the so-called heat assisted magnetic recording (HAMR) technique, a new approach widely considered to be the next hard disk drive technology [14,15]. The BM in pure α-Cr_2O_3 is a well-defined concept that has triggered a lot of work on direct observations and applications. It is also well known that alloying of materials is a crucially important pathway towards property optimization for application purposes. However, it still remains an open fundamental question whether the BM is robust with respect to alloying chromia with another oxide material. The persistence of the surface magnetism should happen only if the magnetoelectricity remains robust against alloying and thus space-inversion and time-reversal symmetries remain broken, while their combined effect is still a symmetry operation for the resulting alloy [16]. α-Cr_2O_3 adopts the corundum crystal structure (space group $R\bar{3}c$), consisting of hexagonal close-packed layers of O atoms with two thirds of the octahedral sites being occupied by Cr^{3+} ions. The oxygen atoms follow an hcp stacking, while the chromium atoms exhibit an *abcabc* stacking sequence as found in fcc lattices [17]. A sketch of this structure is shown in Fig. 1(a). Below its critical temperature, the system exhibits antiferromagnetic order, with a spin ordering $+ - + -$ along the rhombohedral c-axis direction, which is also the easy axis of magnetization (magnetic point group $\bar{3}'m'$). Figure 1(b) shows a cartoon of the spin structure along the c axis. α-Al_2O_3 in its single-crystalline form, sapphire, has been demonstrated to allow for epitaxial growth of chromia films due to the advantage of structural isomorphism and relatively low lattice mismatch, given that $|\Delta a|/a(Al_2O_3) = 4.0\%$ and $|\Delta c|/c(Al_2O_3) = 4.6\%$ [8,10,12,13,18]. Correspondingly, $Cr_{2-x}Al_xO_3$ alloy films with (0001) surface orientation are a most suitable test case for the investigation of structural and magnetic properties, especially in terms of the robustness of boundary magnetization, which needs more exploration [19–22]. In this work, we present a detailed study of the structural and magnetic properties of epitaxial $Cr_{2-x}Al_xO_3$ alloys in the composition range of $x = 0 - 0.6$. Our

---

*Corresponding author: l.fallarino@nanogune.eu
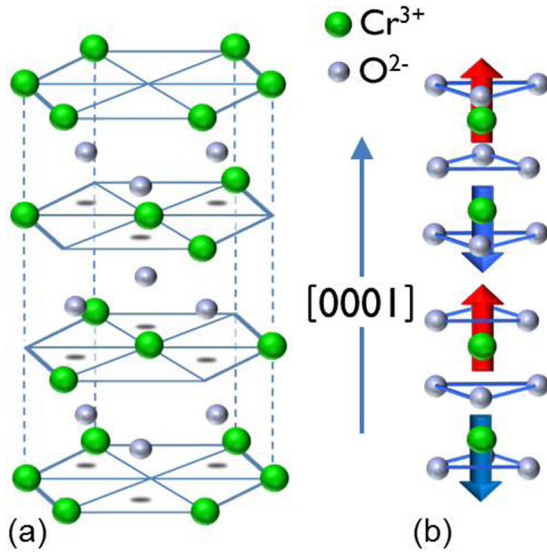
FIG. 1. (Color online) (a) Corundum crystal structure of α-Cr_2O_3; (b) schematic of the antiferromagnetic (AFM) spin order. In zero magnetic field, the chromium spins are aligned antiparallel along the [0001] direction (c axis).

experimental findings corroborate hereby that the observed out-of-plane remanent magnetic moment originates from the sample boundaries rather than the bulk of the samples, independent from the specific concentration. Previously, the surface nature of this magnetic moment was proven for the parent compound chromia by means of surface sensitive techniques, specifically with direct experimental evidence using x-ray magnetic circular dichroism–photoemission electron microscopy (XMCD-PEEM) [10], spin-polarized inverse photoemission [10], and spin-polarized photoemission [8]. The remainder of the paper proceeds as follows. We describe our experimental details in Sec. II. Then in Sec. III A, the identification of the crystal structure and the evaluation of the lattice parameters are presented. In Sec. III B, the experimental results of the magnetic characterization are shown and discussed. Section IV provides a summary of the here accomplished results and the conclusions that can be drawn from them.

II. EXPERIMENTAL METHODS

$Cr_{2-x}Al_xO_3$ thin films were deposited on double-side-polished, 330-μm-thick c-Al_2O_3 (0001) substrates. The conventional sputter deposition method for the production of Cr_2O_3 is dc reactive sputtering of chromium targets under mixed argon and oxygen gas flow at high temperature [23]. Despite commonly obtaining the desired stoichiometry after optimizing the process parameters, very often the presence of oxygen flow results in unsteady deposition rates as well as target poisoning for this type of approach. Therefore, the fabrication of oxide alloys and especially the control of their elemental composition via conventional reactive sputtering are problematic, and generally exhibit rather limited reproducibility. In order to avoid these complications, sintered stoichiometric Cr_2O_3 and Al_2O_3 ceramic disk targets (99.9% pure) were utilized in our deposition process via

radio frequency (rf) magnetron cosputtering of both materials simultaneously. Before deposition, c-Al_2O_3 substrates were ultrasonically cleaned using acetone, methanol, and de-ionized water for 5 min each in successive steps. After that, the c-Al_2O_3 substrates were placed first into the load lock chamber of our sputter system, and then transferred into the sputter chamber, which was kept under UHV conditions with a base pressure of better than 3×10^{-6} Pa. Deposition and codeposition processes were started only after presputtering the oxide targets for at least 5 minutes with the shutters of the guns completely closed. In the initial part of this presputter process, a 2 W/s time ramp was followed in order to reach the desired deposition power. All samples were then deposited at room temperature (RT), using a pressure of 4.0×10^{-1} Pa, a plasma power of 250 W for the Cr_2O_3 target, and a varying power between 50 and 165 W for the Al_2O_3 target, in order to access the intended composition range of $x = 0 - 0.6$. For all film compositions, the film thickness was fixed at 100 nm. In previous studies, it was shown that a combination of RT depositions with high-temperature annealing is an effective method for the growth of epitaxial Cr_2O_3 thin films [17,18,21,24,25]. Thus, our as-grown samples were recrystallized via *ex situ* thermal annealing in vacuum (pressure <3 Pa) for 1 h at 1000 °C in an external furnace (carbolite wire wound single-zone tube furnace). It is worthwhile to mention that *in situ* annealing and high-temperature deposition approaches were explored as well, but with unsatisfactory results, which we ascribe to the fact that our deposition system only allows temperatures of up to 850 °C. The nominal doping content x has been determined by thorough deposition rate calibrations via x-ray reflectivity (XRR), with a relative error of smaller than 0.02 in the entire composition range explored here. The nominal sample composition was verified via energy-dispersive x-ray spectroscopy (EDX) measurements on our film samples before and after the heat treatment. Structural analysis of our thin films was done via x-ray diffraction (XRD) and XRR measurements, utilizing a PANalytical X'Pert Pro diffractometer with Cu $K\alpha$ radiation. Magnetization measurements were performed using a commercial Quantum Design SQUID-VSM magnetometer.

III. RESULTS AND DISCUSSION

A. Structural analysis

In order to identify the crystal structure and to determine the lattice parameters, θ-2θ scans were performed in two different geometries: the coplanar geometry, with the scattering plane normal to the sample surface, and noncoplanar geometry, with the scattering plane normal to the investigated crystal plane, which is accessible via tilting the surface normal by an angle χ with respect to the scattering plane [26]. The in-plane orientation relationship between the substrates and our epitaxial thin films were studied by means of XRD ϕ scans at the $Cr_{2-x}Al_xO_3$ {10–14} poles and for reference purposes, at the Al_2O_3 {10–14} poles via full 2π rotation measurements. Figure 2(a) shows the coplanar XRD θ-2θ patterns for the $x = 0$ sample, i.e., pure Cr_2O_3. After the rf sputter deposition at room temperature, a strong and narrow peak at $2\theta = 41.68°$, corresponding to the Al_2O_3 substrate (0006) diffraction is visible in the XRD θ-2θ scan accompanied by a weak and fairly
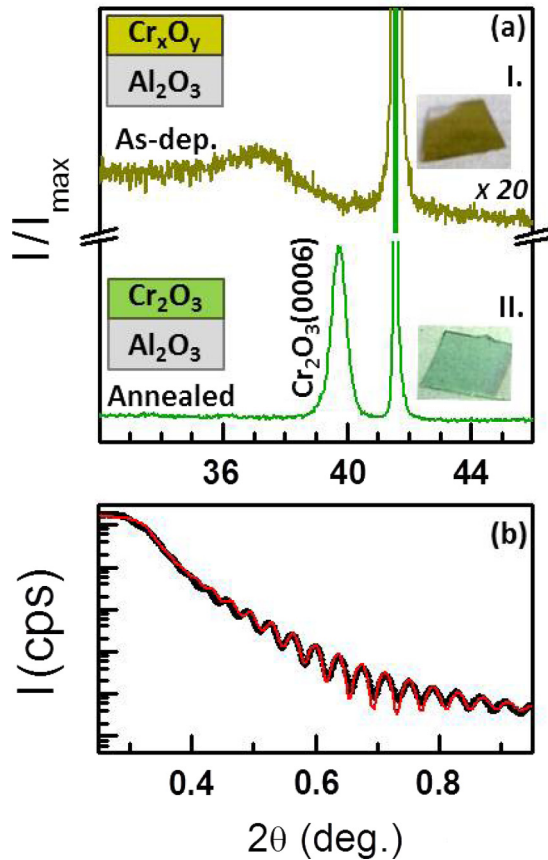
FIG. 2. (Color online) (a) XRD θ-2θ pattern of a 100-nm-thick film in the as-deposited state and after 1000 °C annealing. All films are deposited onto sapphire (0001) substrates, giving rise to the peak at $2\theta = 41.68°$. On the right-hand side, photos of exemplary samples are shown in the as-deposited (inset I) and 1000 °C annealed state (inset II). A sketch of the cross section of the as-deposited (annealed) sample is given in the left top (bottom) part. (b) Small-angle x-ray reflection curve measured for a 100-nm-thick Cr_2O_3 film. The (red) solid line represents the least-squares fit achieved with the PANanalytical X'Pert Reflectivity software.

FIG. 3. (a) XRD θ-2θ scans of 100-nm-thick $Cr_{2-x}Al_xO_3$ films of varying Al_2O_3 concentration x, showing the (0006) reflections. The Al_2O_3 (0006) peaks at $2\theta = 41.68°$ come from the substrate in each case. (b) XRD θ-2θ scans of 100-nm-thick $Cr_{2-x}Al_xO_3$ samples of varying Al_2O_3 concentration x, showing the (10–14) reflections. The Al_2O_3 (10–14) peaks at $2\theta = 35.15°$ come from the substrate in each case.

broad peak around $2\theta = 37°$. This broad structure indicates that for the pure Cr-oxide case here, the as-grown films contain a small crystallized CrO_3 minority phase, while our EDX measurements reveal that our films consist primarily of Cr_2O_3, which is either amorphous or nanocrystalline. After *ex situ* thermal annealing at 1000 °C, the heterogeneous phase has been transformed into the sesquioxide Cr_2O_3 phase, as demonstrated by the intense and sharp diffraction peak at $2\theta = 39.75°$, corresponding to the (0001) surface orientation of the chromia film. The thermal "metamorphosis" of the sample is further supported by the absence of any other peak in the XRD scan and visually by the appearance of a characteristic green color, as seen in Fig. 2 (inset II). The results for all other $Cr_{2-x}Al_xO_3$ compounds investigated here are very similar in terms of their structural and compositional evolution during the annealing process. In order to monitor for possible interface diffusion of Al atoms from the substrate into the thin films during the high-temperature sample processing, x-ray reflectivity measurements were performed after the
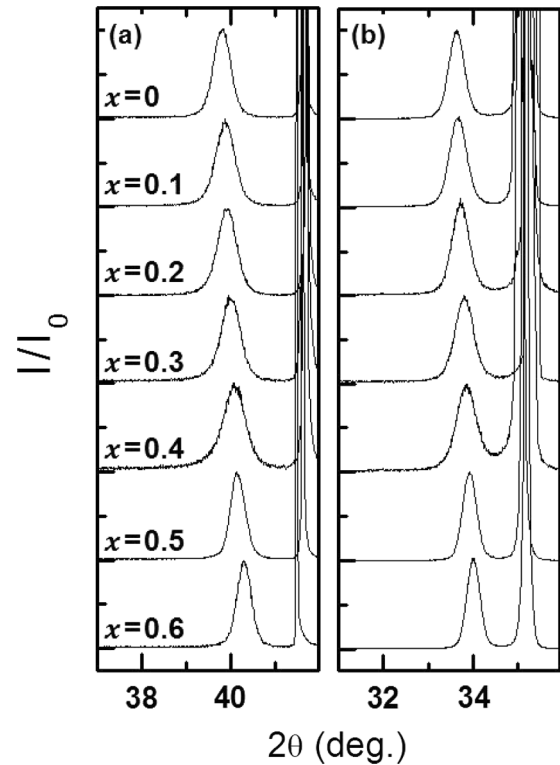
high-temperature annealing step. Figure 2(b) shows the XRR data for the pure Cr_2O_3 sample together with the fitting result (red straight line) obtained by the PANanalytical X'Pert Reflectivity software. We observe a large number of very well-defined Kiessig fringes, due to the high chemical gradient at the interface, indicating very limited interface diffusion. From the data fit, we have determined that the Cr_2O_3 film has a thickness of 101.40 ± 2.10 nm and an interface roughness of only 0.32 ± 0.11 nm. Very similar XRR data have been measured for all our samples, with an estimated interface roughness of less than 0.5 nm in all cases. In order to achieve consistently good epitaxy, we utilized 1000 °C as annealing temperature for all alloy samples after the initial rf sputter deposition of the films at room temperature [12,13]. Figure 3(a) shows the coplanar XRD θ-2θ patterns for the entire set of samples, normalized to I_0, which is the intensity of the $Cr_{2-x}Al_xO_3$ (0006) peak in each individual scan. Beside the reference substrate peaks, the entire set of data shows well-defined $Cr_{2-x}Al_xO_3$ (0006) peaks of nearly uniform width without the appearance of any other crystallographic diffraction peak. Figure 3(b) shows the noncoplanar XRD θ-2θ patterns normalized to I_0, which is the intensity of the $Cr_{2-x}Al_xO_3$ (10-14) peak in each individual scan. Also for this XRD scan, only $Cr_{2-x}Al_xO_3$ (10–14) peaks of consistently narrow width associated with the (0001) surface orientation were found, in addition to the substrate signal. Thus, our
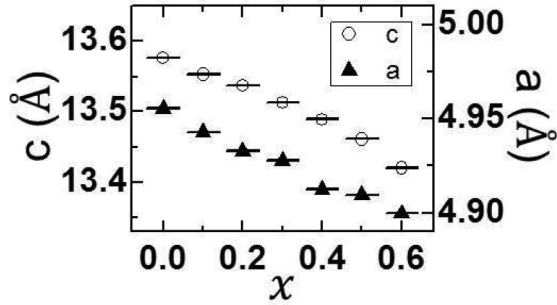
FIG. 4. Al_2O_3 concentration x dependence of the $Cr_{2-x}Al_xO_3$ lattice parameters, determined from XRD θ-2θ measurements.
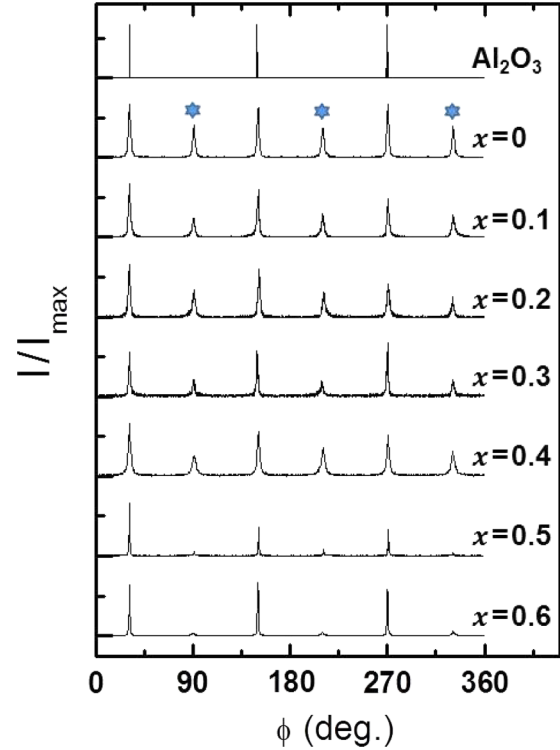

FIG. 5. (Color online) XRD ϕ scans at the 2θ pole of the (10–14) planes for various $Cr_{2-x}Al_xO_3$ thin films and for the Al_2O_3 substrates. The stars mark the twinned domain positions.

structural sample analysis verifies the persistence of the original corundum crystal structure in the entire set of samples, necessary for the survival of the boundary magnetization [9]. The ionic radius of the Cr^{3+} is larger than that of Al^{3+}, so that the distance between the lattice planes decreases upon increasing the amount of alumina in the alloy [22]. Correspondingly, the XRD peak positions in our samples shift from diffraction angles of 39.75° (0006) and 33.6° (10-14) for the pure Cr_2O_3 towards the Al_2O_3 (0006) and (10–14) diffraction peaks upon increasing x. This x-dependent peak shift in the absence of significant broadening verifies the simple Cr^{3+} substitution by Al^{3+} and the corresponding formation of isovalent solid solutions–type samples in the entire range between $x = 0$ and $x = 0.6$. Also, the XRD data verify the epitaxial quality of the growth process, which allowed for the fabrication of chromia-alumina alloy films with c-axis surface orientation in the here investigated concentration range. The lattice constants a and c of our alloy films were measured from the peak positions in the θ-2θ scans and are plotted in Fig. 4. Both a and c decrease linearly with x, further corroborating the smooth tunability of our high-quality growth process. The agreement with lattice constants published for polycrystalline bulk $Cr_{2-x}Al_xO_3$ alloy samples is very good, as can be seen from the comparison in Table I [20,22]. For the purpose of a further sample comparison, Fig. 5 shows experimental results of XRD ϕ scans for the entire range of alloy compositions investigated here. The substrate gives rise to three peaks separated by 120°, while the $Cr_{2-x}Al_xO_3$ films exhibit six peaks, separated by 60°. Since the corundum structure has

threefold symmetry along the [0001] direction, the occurrence of the sixfold symmetry indicates that the films consist of twinned domains (marked by the stars in Fig. 5), which have been previously reported to occur during thermal annealing in pure chromia [17,18,27]. The intensity of the twinned domain peaks decreases with the Al content, disappearing almost entirely for the $x = 0.6$ sample. To visualize this effect more clearly, Fig. 6 shows the quantity s, the ratio between the average XRD intensity of the twinned domains normalized to the untwinned one, $s = I_{Twinned}/I_{Untwinned}$. As we can see, s decreases substantially for larger x, which means that we actually achieve an improvement of the epitaxial growth quality by alloying Cr_2O_3 with Al_2O_3. As we will see later, this aspect turns out to be of importance for the boundary

TABLE I. Comparison between bulk lattice parameters and values found in this work.

Sample composition		This work		Reference values[a]		Reference values[b]	
Al_2O_3 at.%	Cr_2O_3 at.%	a (nm)	c (nm)	a (nm)	c (nm)	a (nm)	c (nm)
0	100	0.4955	1.3578	0.4958	1.3594	0.4954	1.3573
5	95	0.4943	1.3553				
10	90	0.4932	1.3537	0.4934	1.3502	0.4939	1.3530
15	85	0.4927	1.3513				
20	80	0.4912	1.3489	0.4910	1.3424	0.4922	1.3471
25	75	0.4909	1.3461				
30	70	0.4899	1.3422	0.4889	1.3356	0.4903	1.3417

[a]Reference [20].
[b]Reference [22].
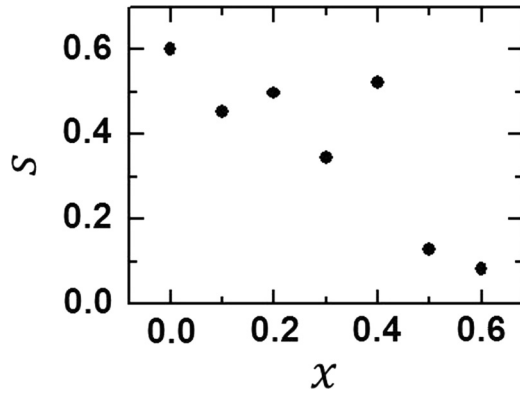
FIG. 6. Al_2O_3 concentration x dependence of s, the ratio between the average XRD intensity of the twinned domain signal $I_{Twinned}$ and the untwinned domain signal $I_{Untwinned}$, both measured for the (10–14) plane.

magnetization, because the magnetic surface polarization depends on the ratio of twinned to untwinned domains [27].

B. Magnetic characterization

The characteristics of ferromagnetic materials are most frequently given in terms of their m vs H isothermal hysteresis loop. Because of the weak magnetic signal of interest here, however, any background susceptibility contribution from our samples can easily mask the low moment of the BM. In order to suppress these noise sources, it was necessary to measure the magnetic signal in the complete absence of any applied magnetic field, a condition that was achieved by quenching [28] the superconducting magnet of our magnetometer prior to every measurement sequence. Correspondingly, we have utilized a rather specific T- and H-dependent measurement protocol, consisting of a zero-field heating (ZFH) magnetization measurement sequence, starting at $T = 100$ K and following up to $T = 350$ K, after first high-field cooling (FC) the sample from $T = 350$ K down to $T = 100$ K. Details of this measurement procedure have been published elsewhere [12,13,29]. Figure 7 shows the resulting temperature dependence of the out-of-plane remanent magnetic moment m for the entire set of our epitaxial $Cr_{2-x}Al_xO_3$ alloy films after prior FC in an applied magnetic field of $\mu_0 H = 7$ T. All data show a positive magnetization value at low temperature due to the positive magnetic field applied during FC, which leads to the selection of a state with positive BM. Upon increasing the temperature, the remanent signal decreases continuously until it disappears at a clearly defined temperature. For higher temperatures, no magnetization can be observed anymore in the absence of an external magnetic field, because the boundary magnetization disappears simultaneously with the antiferromagnetically ordered state for each of the $Cr_{2-x}Al_xO_3$ alloy films. In this high-temperature regime, all samples show a paramagnetic (PM) behavior, including a vanishing remanent magnetization. For the purpose of a side-by-side comparison of the m vs T data of all samples in Fig. 7, the magnetic signal was normalized by the respective moment measured at $T = 0.9\, T_N(x)$, called m_0, with $T_N(x)$ being the critical temperature of the antiferromagnetic order in the $Cr_{2-x}Al_xO_3$
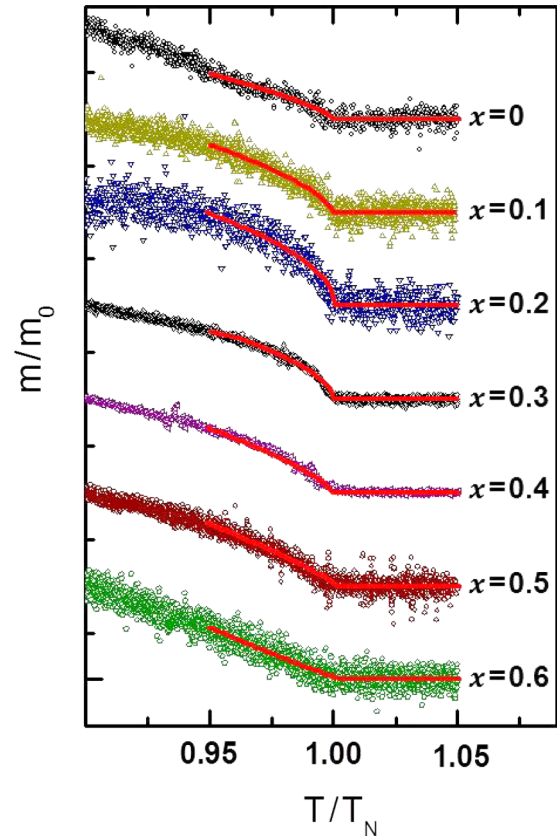

FIG. 7. (Color online) Temperature dependence of the remanent boundary magnetization in $Cr_{2-x}Al_xO_3$ thin films of varying Al_2O_3 concentration x. The (red) lines show least-squares fits to Eq. (1) for each of the sample data sets.

alloy film of composition x. $T_N(x)$ itself, together with the temperature critical exponent β, was determined by fitting the experimental data in the temperature range $0.95\, T_N(x) < T < 1.05\, T_N(x)$ to the power law function:

$$m(T) = A \times (T_N - T)^\beta \times H(T_N - T), \qquad (1)$$

with $H(T_N - T)$ being the Heaviside function. Hereby, the critical exponent β, T_N, and a scaling factor A were utilized as fit parameters. Figure 7 shows the fitting results as (red) solid lines in direct comparison to the experimental data. In each case, we find excellent agreement between the experimental data and the least-squares fit according to Eq. (1). The dependence of the BM on the AF ordering allows us to identify the critical temperatures. This is a crucial observation for our epitaxial $Cr_{2-x}Al_xO_3$ film samples, because it means that substituting Cr atoms by Al atoms destroys neither the AFM magnetic order, nor the BM. The extracted values for the critical temperature $T_N(x)$ are shown in Fig. 8. For pure Cr_2O_3, i.e., $x = 0$, T_N is very close to the value for bulk Cr_2O_3, namely $T_N = 307$ K, and also very similar to previously reported values for samples of comparable thickness, grown by different deposition techniques [8,10,30]. In the case of the alloy films, $T_N(x)$ decreases upon introducing Al into the Cr_2O_3 lattice and does so in an almost linear fashion with the Al concentration x. The reduction of $T_N(x)$ upon increasing x is not surprising, given that Al^{3+} ions reduce the AFM exchange
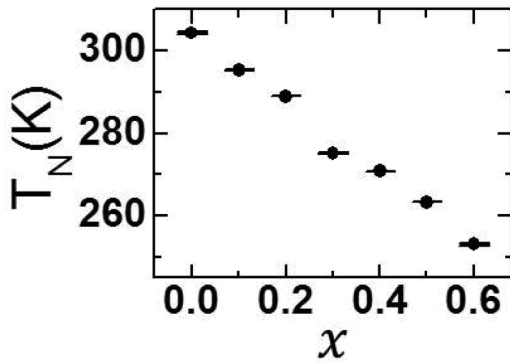
FIG. 8. Al_2O_3 concentration x dependence of the extracted critical temperature T_N values.

interaction of the crystal. Quantitatively, the decrease of the critical temperature is in accordance with the results observed for bulk polycrystalline $Cr_{2-x}Al_xO_3$ samples [21,22]. The extracted β values for the critical exponent, together with the associated errors estimated from each of the least-squares fits, are plotted in Fig. 9 as a function of the Al content x, along with critical exponents for the 3D Heisenberg ($\beta = 0.365$) and the 3D Ising ($\beta = 0.3265$) models and a prediction made for the critical exponent of the surface of a 3D Ising system ($\beta = 0.78$) [31–33]. Despite notable variations in between the extracted critical exponents for our samples, all β values are consistently and substantially larger than what one would expect for three-dimensional systems. On the other hand, the average value $\bar{\beta} = 0.73 \pm 0.07$ that we have determined from our experiments is consistent within the statistically estimated error with the critical exponent value $\bar{\beta}_S = 0.78 \pm 0.02$ that was predicted by Binder for the surface magnetization of a 3D Ising model. Thus, the critical behavior we observe in our samples here can also be considered as corroborating the large body of experimental evidence that identifies the remanent ferromagnetic signal observed in epitaxial Cr_2O_3 and $Cr_{2-x}Al_xO_3$ films as boundary magnetization [10–13]. The estimated error that we assigned to the average critical exponent $\bar{\beta}$ above is the standard deviation of the mean. Under
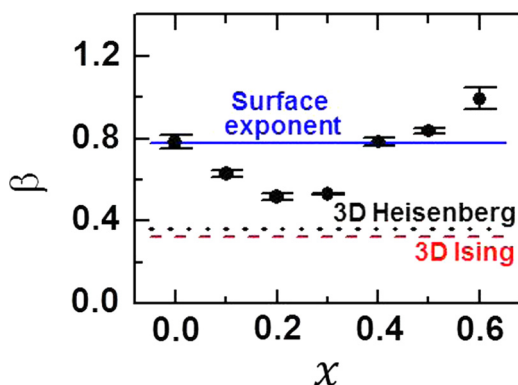

FIG. 9. (Color online) Al_2O_3 concentration x dependence of the extracted critical exponent β. The straight (blue) line indicates the surface exponent predicted by Binder *et al.*, the (black) dotted line indicates the 3D Heisenberg model value, and the dashed (red) line shows the 3D Ising model β [31–33].
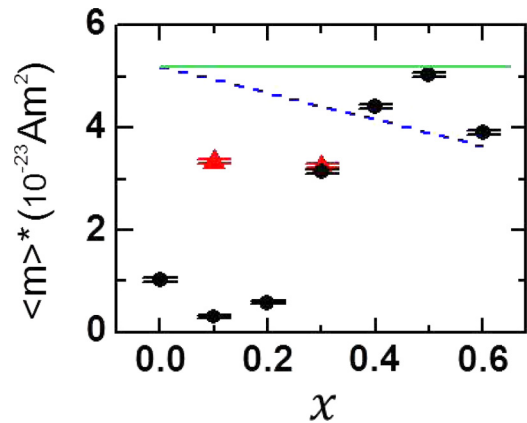

FIG. 10. (Color online) Al_2O_3 concentration x dependence of the absolute moment per hexagonal unit area $\langle m \rangle^*$. The (black) dots represent the values at 100 K in the absence of any magnetic field during the measurement, after prior magnetic field cooling. The (red) triangles represent values measured at 100 K in the presence of a 200 mT magnetic field after prior field cooling. The straight (green) line marks the expected value for a fully polarized hexagonal unit cell at the surface for pure Cr_2O_3 [8]. The dashed (blue) line represents the expected value for a fully polarized hexagonal surface unit cell for a randomly mixed $Cr_{2-x}Al_xO_3$ alloy under the assumption that Al does not carry any magnetic moment.

the assumption of a purely statistical Gaussian distribution for the observed β values, one would correspondingly expect that 68% of all data fall into the interval defined by $\bar{\beta} \pm \sigma$, with $\sigma = 0.17$ being the standard deviation. Experimentally, this is almost fulfilled with four out of seven experimental β values being located in this range. However, the data in Fig. 9 do not appear to represent a random sequence, but instead follow a superimposed parabolic behavior, with a minimum occurring for $x = 0.2$, which suggests the existence of an underlying doping dependence of β. This is especially evident if one considers the rather small estimated error for each individual data point. Thus, in assessing the reliability of our data analysis, one has to keep in mind that the experimentally determined mean value $\bar{\beta} = 0.73 \pm 0.07$ and its associated standard deviation are derived without the explicit consideration of an x-dependent critical exponent β.

In order to further investigate this systematic variation of the experimentally determined critical exponents with the Al concentration x, the absolute moment per hexagonal surface unit, $\langle m \rangle^*$, was determined. Figure 10 shows our experimental $\langle m \rangle^*$ values, (black) circular dots, as a function of x. The (green) straight line represents the value for a fully polarized hexagonal Cr_2O_3 unit cell at the surface, which was estimated by Binek *et al.*, as an expected limit for the maximum possible BM value [8]. The dashed (blue) line represents the corresponding value for a full polarized hexagonal $Cr_{2-x}Al_xO_3$ unit cell under the assumption that Al does not carry any magnetic moment and that the surface layer has the exact same alloy concentration as the film on average. The samples for small x show small $\langle m \rangle^*$ values, while the high-x materials exhibit $\langle m \rangle^*$ values close to the theoretical expectation for a full uniform surface magnetization. It is hereby important to notice that the entire set of observed

$\langle m \rangle^*$ values never exceeds the theoretical BM threshold. To understand the strong x dependence of $\langle m \rangle^*$, we recall from our structural analysis of the samples that films with low Al concentration possess a lower crystal quality. Specifically, the low-x samples exhibit a far higher presence of twinned crystallographic domains if compared to the Al-rich, high-x samples, for which the twinning almost disappears. As reported before, twinned domains can cause the occurrence of different magnetic sublattices at the surface [27]. This suggests a strong connection between twinning and the observable remanent BM: the lower the percentage of twinning is, the more stable will be the magnetization at the boundary after the field cooling procedure. In order to test this hypothesis, in addition to its obvious consistency with the $\langle m \rangle^*$ vs x data in Fig. 10, we have measured the $m(T)$ behavior following the procedure applied for the data in Fig. 7, but in the presence of a positive axial field $\mu_0 H = 0.2$ T for the $x = 0.1$ and $x = 0.3$ samples. From these measurements, $\langle m \rangle^*$ values have been determined in the presence of a magnetic field, which are shown in Fig. 10 as (red) triangles. The $x = 0.3$ sample shows a value that is nearly unchanged from its already large remanent value, which means that almost the entire saturation magnetization is retained in the measurement procedure when the field is removed after field cooling in $\mu_0 H = 7$ T. On the other hand, the $x = 0.1$ sample shows a substantially enhanced $\langle m \rangle^*$ value with the applied field, bringing both samples to nearly identical $\langle m \rangle^*$ levels. This can be explained if one assumes that, once the magnetic field is switched off upon the completion of the FC sequence, the surface develops a magnetic multidomain state caused by the twinned crystal domains, but still has a majority of the surface moments pointing in the direction of the originally applied field during the FC sequence. As a consequence, the evaluated exponents β for the low-Al-concentration samples must be considered to be less reliable, because they are extracted from measurements on multidomain states, even if there still is a net polarized state that follows the previously applied saturation field.

IV. CONCLUSIONS

We have investigated the effect of α-Al$_2$O$_3$ doping on the structural and magnetic properties of the magnetoelectric antiferromagnet α-Cr$_2$O$_3$. The findings demonstrate the fundamental viability of tuning the critical temperature of α-Cr$_2$O$_3$-based magnetoelectric antiferromagnets by means of alloying, while preserving the symmetry of the antiferromagnetic order state, as well as the associated existence of the BM. Unlike the two well-established and specific approaches focused on engineering the critical temperature of chromia, i.e., strain induced and anion impurities substitutional doping, we introduce here a suitable pathway towards the optimization and preservation of the BM properties by alloying

with isostructural materials. Specifically, we demonstrate the growth of high-quality corundum Cr$_{2-x}$Al$_x$O$_3$ (0001) thin films in the concentration range between $x = 0$ and $x = 0.6$, successfully verifying the suitability of the hybrid growth procedure for chromia-based alloy fabrication, which extends our previous work on high-quality pure α-Cr$_2$O$_3$ thin film growth [12,13]. The samples show a linear variation of the lattice constants a and c with x, as well as a monotonic decrease of the Néel temperature with x similar to the results of studies on bulk polycrystalline alloy samples [19–22]. In contrast with those studies, the highly oriented epitaxial nature of our alloy film samples allows the use of the boundary magnetization as a probe to study the magnetic transition. Here, we were able to directly evaluate the critical exponent and the absolute magnetization level of the BM, without the support of magnetic heterostructures, which are both in good agreement and consistent with the predicted values [8,31–33]. Although the boundary magnetization is intimately coupled to the bulk antiferromagnetic order parameter, we could show that the critical behavior of the boundary magnetization deviates from the critical behavior of the bulk antiferromagnetic order parameter. Even given the apparent x dependence of the surface critical exponent, the lowest limit for the estimated critical exponents is still significantly larger than the one expected for the bulk. This corroborates the surface nature of the FM signals of the samples and confirms the robustness of the boundary magnetization state upon alloying with isostructural diamagnetic alumina. We expect that our findings extend in general to other magnetoelectric antiferromagnetic materials and alloys as long as lattice structure and symmetries are equally preserved, which should ultimately enable technological applications of the BM phenomenon by combining its unique properties with a broad material class for unique functional devices.

[1] I. E. Dzyaloshinskii, Sov. Phys. JETP **10**, 628 (1959).

[2] D. N. Astrov, Sov. Phys. JETP **11**, 708 (1960); **13**, 729 (1961).

[3] V. J. Folen, G. T. Rado, and E. W. Stalder, Phys. Rev. Lett. **6**, 607 (1961).

[4] T. H. O'Dell, *The Electrodynamics of Magneto-Electric Media* (North-Holland, Amsterdam, 1970).

[5] M. Fiebig, J. Phys. D: Appl. Phys. **38**, R123 (2005).

[6] T. J. Martin and J. C. Anderson, IEEE Trans. Magn. **2**, 446 (1966).

[7] P. Borisov, A. Hochstrat, X. Chen, W. Kleemann, and Ch. Binek, Phys. Rev. Lett. **94**, 117203 (2005).

[8] X. He, Y. Wang, N. Wu, A. N. Caruso, E. Vescovo, K. D. Belashchenko, P. A. Dowben, and Ch. Binek, Nat. Mater. **9**, 579 (2010).

[9] K. D. Belashchenko, Phys. Rev. Lett. **105**, 147204 (2010).

[10] N. Wu, X. He, A. L. Wysocki, U. Lanke, T. Komesu, K. D. Belashchenko, Ch. Binek, and P. A. Dowben, Phys. Rev. Lett. **106**, 087202 (2011).

[11] S. Cao, X. Zhang, N. Wu, A. T. N'Diaye, G. Chen, A. K. Schmid, X. Chen, W. Echtenkamp, A. Enders, Ch. Binek, and P. A. Dowben, New J. Phys. **16**, 073021 (2014).

[12] L. Fallarino, A. Berger, and Ch. Binek, Appl. Phys. Lett. **104**, 022403 (2014).

[13] L. Fallarino, A. Berger, and Ch. Binek, Phys. Rev. B **91**, 054414 (2015).

[14] J. U. Thiele, S. Maat, and E. E. Fullerton, Appl. Phys. Lett. **82**, 2859 (2003).

[15] D. Weller, O. Mosendz, G. Parker, S. Pisana, and T. S. Santos, Phys. Status Solidi A, **210**, 1245–1260 (2013).

[16] S. Foner and M. Hanabusa, J. Appl. Phys. **34**, 1246 (1963).

[17] A. Kilian, F. Bernardi, A. Pancotti, R. Landers, A. de Siervo, and J. Morais, J. Phys. Chem. C **118**, 20452 (2014).

[18] S. Y. Jeong, J. B. Lee, H. Na, and T. Y. Seong, Thin Solid Films **518**, 4813 (2010).

[19] Y. Kitaoka, K. Nakamura, T. Akiyama, and T. Ito, J. Cryst. Growth **362**, 42 (2013).

[20] F. Bondioli, A. M. Ferrari, C. Leonelli, and T. Manfredini, J. Am. Ceram. Soc. **83**, 2036 (2000).

[21] V. A. Drebushchak and A. I. Turkin, J. Therm. Anal. Calorim. **90**, 795 (2007).

[22] S. H. Yang, S. J. Liu, Z.H. Hua, and S. G. Yang, J. Alloys Compd. **509**, 6946 (2011).

[23] T. Ashida, T. Oida, M. Shimomura, N. Nozaki, T. Shibata, and M. Sahashi, Appl. Phys. Lett. **104**, 152409 (2014).

[24] H. Mashiko, T. Oshima, and A. Ohtomo, Jpn. J. Appl. Phys. **51**, 11PG11 (2012).

[25] F. S. Stone and J. C. Vickerman, Trans. Faraday Soc. **67**, 316 (1971).

[26] In the noncoplanar configuration, the diffraction measurement parameters were optimized only for the epitaxial alloy film reflections. Therefore, the Al_2O_3 (10–14) diffraction peaks exhibit a certain level of variation without, however, affecting the reliability of the experimental data.

[27] N. Iwata, T. Kuroda, and H. Yamamoto, Jpn. J. Appl. Phys. **51**, 11PG12 (2012).

[28] The quenching process of the superconducting magnet coil in our SQUID-VSM magnetometer consists of two steps: first, the electrical current through the superconducting solenoid coil is set to zero and in a second step, the solenoid coil is heated above its superconducting transition temperature to eradicate any trapped flux.

[29] M. Street, W. Echtenkamp, T. Komesu, S. Chao, P. A. Dowben, and Ch. Binek, Appl. Phys. Lett. **104**, 222402 (2014).

[30] X. He, W. Echtenkamp, and C. Binek, Ferroelectrics **426**, 81 (2012).

[31] K. Binder and P. C. Hohenberg, Phys. Rev. B **9**, 2194 (1974).

[32] K. Binder and D. P. Landau, Phys. Rev. Lett. **52**, 318 (1984).

[33] D. P. Landau and K. Binder, Phys. Rev. B. **41**, 4633 (1990).